

# Calibration of Millimeter-wave Channel Sounders for Super-resolution Multipath Component Extraction

Peter B. Papazian<sup>1</sup>, Jae-Kark Choi<sup>2</sup>, Jelena Senic<sup>1</sup>, Peter Jeavons<sup>1</sup>, Camillo Gentile<sup>2</sup>, Nada Golmie<sup>2</sup>, Ruoyu Sun<sup>1</sup>,  
David Novotny<sup>1</sup>, Kate A. Remley<sup>1</sup>

National Institute of Standards and Technology (NIST), Communications Technology Laboratory

<sup>1</sup>Boulder, Colorado, USA <sup>2</sup>Gaithersburg, Maryland, USA

**Abstract**—Millimeter-wave communication systems will rely on highly directional antennas to compensate for the greater pathloss expected in their frequency bands of operation. Hence, electronic beamforming will form a cornerstone for the technology. For the effective design of these systems, accurate estimation of the multipath component characteristics of the environment is essential, in particular their three-dimensional angle-of-arrival. Super-resolution techniques enable extracting these components with high fidelity, even in the presence of diffuse scattering. Applying these techniques, however, requires precision calibration of our 28, 60, and 83 GHz channel sounders. This paper outlines calibration procedures implemented to deliver such precision. Specifically, we account for impulse-response distortion stemming from internal system reflections and linear distortion by RF components. We also characterize the phase centers and complex antenna patterns of the receiver array elements, and gauge the drift of our synchronization clocks.

**Keywords**—Cellular communication; channel sounder; millimeter-wave communication; propagation channel; radio channel; wireless system

*Publication of the United States government, not subject to copyright in the U.S.*

## I. INTRODUCTION

Millimeter-wave communication systems will employ directional antennas with beamwidths on the order of degrees, rather than tens of degrees [1]. Because of their high gain, typically 25-40 dBi, these *pencilbeams* can compensate in part for the greater pathloss expected in the associated frequency bands of operation. To provide for ubiquitous coverage, electronic steering and/or spatial multiplexing will be required at the mobile station. For effective design of these technologies, accurate estimation of the multipath component characteristics of the environment is essential, in particular their three-dimensional (azimuth and elevation) angle-of-arrival (AoA). Super-resolution techniques provide for extracting these components with high fidelity, even in the presence of diffuse scattering. Applying these techniques, however, requires precise calibration, especially when operating in the frequency regime of the 28, 60, and 83 GHz systems.

The scope of this paper is to outline calibration procedures implemented to deliver such precision. In the next section, we provide an overview of the channel sounder architecture common to all three systems. Section III is the main section, in it, we explain how to compensate for impulse-response

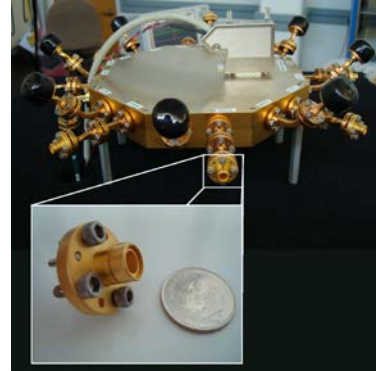


Figure 1. 83 GHz antenna array with inset of scalar feed horn. Eight straight elements (no covers) and eight slanted elements.

distortion due to internal system reflections and linear distortion caused by the RF components. In order to extract AoA accurately, the positions and phase centers of the receiver array elements must be measured to within fractions of a wavelength. This is difficult when the wavelength at 83 GHz is only 3.6 mm. Thus, we describe a procedure using a NIST laser-tracking system. Finally, we outline our antenna calibration and characterize the clock drift. In Section IV, we describe how the SAGE algorithm, used to extract the multipath components, incorporates the calibration measurements and present some results.

## II. CHANNEL SOUNDER ARCHITECTURE

The three NIST mm-wave channel sounders share common hardware sections such as the arbitrary waveform generator, digitizer, timing circuitry, and automated mobile positioning robot. They also use multiplexed scalar feed horn antenna to create antenna arrays. They differ chiefly in the transmitter, where the 83 and 28 GHz channel sounders, effectively have a Single-Input Multiple-Output (SIMO) architecture while the 60 GHz sounder also has Multiple Input (MIMO) and a higher chip rate.

### A. Transmitter

The 83 and 28 GHz systems transmit a periodic 2047-bit pseudorandom noise (PN) code occupying a 2 GHz null-to-null bandwidth. The chip rate is 1 GB/s, translating to a code period of  $2.047 \mu\text{s}$ . The code period determines the maximum range of 600 m and the number of chips per code determines the correlation gain of 66 dB. A 12-bit, 12 GS/s arbitrary

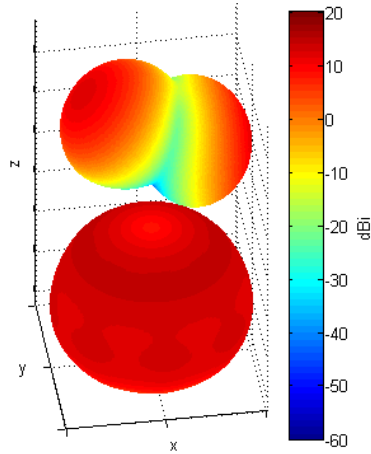


Figure 2. Synthesized antenna patterns for two receiver array elements (top, shifted upwards to avoid overlap) and all 16 elements together (bottom).

waveform generator (AWG) produces a BPSK-modulated IF signal. The AWG allows modification of the transmit waveform: its bit rate and bandwidth can be changed, and pre-distortion filters applied. The IF signal is then upconverted to the appropriate center frequency and the high-side signal is band-pass filtered to remove local-oscillator leakage from the single balanced millimeter-wave mixer. This signal is then amplified and a directional coupler monitors the transmit power at the antenna terminals. An omnidirectional or widebeam transmit antenna is used so all angles-of-arrival can be estimated by the receive antenna array in one fast recording. The 60 GHz system has similar IF components but instead employs an eight-element array at the transmitter so that the angle-of-departure can also be estimated. Other noteworthy differences are the 2 GB/s chip rate and 4 GHz RF bandwidth. For more details concerning the antenna and RF systems, see [2].

### B. Receiver Antenna Array

The key features of the receiver are the antenna array, the fast electronically switched multiplexer (MUX), synchronized timing circuitry, and 40 GS/s IF digitization. Figure 1 shows the 83 GHz array and the MUX. The inset shows one of the 16 scalar feed horn (SFH) antennas. The array is octagonal in shape with one face every 45°. This allows two antennas to be placed side-by-side per face: one pointing straight and the other slanted upwards at 45°. The feed horns have symmetrical Gaussian beam shapes with 45° beamwidth covering most of the upper hemisphere. Synthesized beam patterns are shown in Figure 2: the top for two elements (one straight and one slanted) on opposite sides of the array, each with a boresight gain of 12.2 dB, the bottom is for all 16 elements together. The latter reveals an omnidirectional pattern in azimuth while in elevation the boresight gain is 14.1 dB at 47° and the beamwidth is 87°. The received IF signal is digitized directly and correlation of the transmitted PN pulse is performed in post-processing [3]. While requiring a faster digitizer, this method is three-to-four orders of magnitude faster than analog

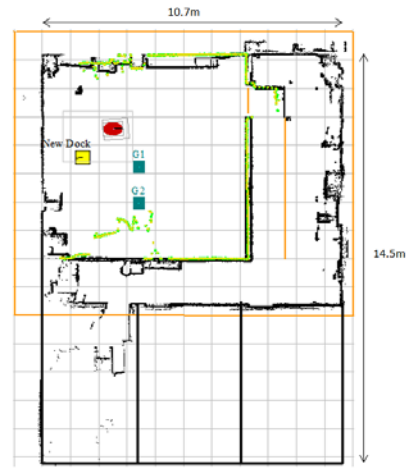


Figure 3. Room floor plan made by navigation system with 1 m grid lines. The red circle indicates the robot position.

sliding-correlation processing because it reduces the measurement period to that of the transmitted code alone. The speed of the antenna MUX allows mobile measurement of angle-of-arrival within the coherence time of the channel.

### C. Robotic Positioning System

The TX-RX system can collect channel impulse response data in a mobile, untethered mode. Indoors, a mobile robot is used to navigate and provide position information. Before a measurement campaign begins, the robot maps an environment such as a room, a series of hallways, or even the entire floor of a building. One such mapping is displayed in Figure 3. Here, the robot is designated with a red oval, the walls and solid surfaces as black lines, and the colored lines indicate what the navigation system can see from its current position. Once the mapping is complete and the measurement campaign begins, the robot is fed a set of two-dimensional waypoints. As it proceeds between waypoints, it collects data at uniformly spaced time intervals while reporting its state, position, heading, and velocity at each. The data collected at each site corresponds to 32 MUX rotations (one rotation encompasses IF digitization of the 16 receive antennas) over a distance of about 10 wavelengths. The routes can be repeated within an accuracy of several centimeters to provide statistics on data repeatability. This accuracy was determined with surveying equipment. The robot can also sense obstacles such as people and avoid them by changing its route or waiting for moving obstacles to pass. Outdoors, GPS localization can be utilized instead.

### D. Timing and Synchronization

Timing and synchronization are maintained with two rubidium clocks, one at the transmitter and the other at the receiver. At the transmitter, the clock's 10 MHz reference is applied to the AWG and the RF section of the upconverter. Before indoor measurements commence each day, the clocks are synchronized through a direct connection of the PPS output of the receiver clock connected to the PPS input of the transmitter clock. Outdoors the PPS synchronization of the clocks can be maintained via GPS if a signal is present. After the clocks are synchronized, a start trigger is sent to the

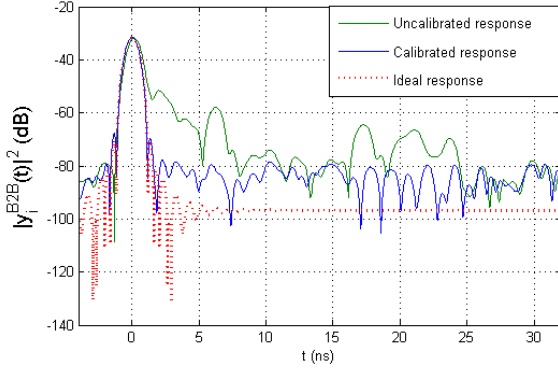


Figure 4. Impulse-response calibration.

receiver from the AWG. This start trigger will synchronize the digitizer trigger and the 4-bit output signal used to switch the MUX between array elements. In this way, the digitizer trigger and antenna switching are synchronized with the transmission of PN codewords. Once the timing circuit is triggered at the receiver, the start trigger cable is disconnected and the receiver can become mobile.

The receiver is able to measure the absolute time-of-arrival plus the clock drift. The receiver timing circuit runs at the bit rate of the transmitter and has an initial divider ratio to create triggers with a granularity of two code periods. This rate is used to switch the antenna elements while a second divider provides triggers to the digitizer at integer multiples of 32 codewords, the equivalent of a single MUX rotation through all 16 antenna elements. By dwelling at each antenna position for two codewords, a complete word is digitized between the finite rise and fall times of the MUX switching. Hence, a total channel measurement (or single rotation) takes  $32 \times 2.047 \mu\text{s} = 65.5 \mu\text{s}$ . This is the minimum time between successive impulse recordings and so dictates the maximum Doppler frequency measurable by the system, 7.6 kHz, limiting Doppler measurement to speeds of 60 mph.

### III. CHANNEL SOUNDER CALIBRATION

The ensuing subsections treat the power and frequency calibrations of the channel impulse responses, how clock drift is gauged, and the characterization of the phase centers and complex antenna patterns of the receiver array elements.

#### A. Channel Impulse Response

Through the post-processing described in Section II.B, the IF-digitized data at the receiver are converted into the *uncalibrated* impulse response of the array elements,  $\hat{y}_i(t), i = 1 \dots 16$ . Each response, in block sequence, is composed from: the transmitted pulse (which is the autocorrelation of the null-to-null PN sequence)  $p(t)$ , the system response and the antenna pattern of the transmitter  $h^{TX}(t)$  and  $g^{TX}$  respectively, the channel response between the transmitter and the element  $h_i(t)$ , the antenna pattern and the system response of the element,  $g_i^{RX}$  and  $h_i^{RX}(t)$ , respectively, plus noise:

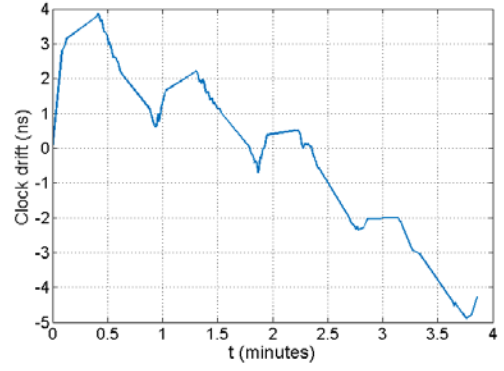


Figure 5. Clock drift when the robot is moving as measured with time-lag properties from the PN correlation function.

$$\hat{y}_i(t) = p(t) * h^{TX}(t) * g^{TX} * h_i(t) * g_i^{RX} * h_i^{RX}(t) + n(t). \quad (1)$$

The purpose of the impulse-response calibration is to deembed the linear  $h^{TX}(t)$  and  $h_i^{RX}(t)$  from (1). To this end, a back-to-back method [3] was used. In this configuration, the antenna port of each transmitter and each receiver element are sequentially connected through a waveguide and a set of variable vane attenuators such that  $g^{TX} = g_i^{RX} = 1$  and  $h_i(t) = \delta(t)$ . A directional coupler monitors the transmitter power at the antenna port by use of a wideband power sensor. The AWG is then configured to transmit the modulated IF signal while operating at full power. The variable attenuators are set to maximum attenuation so that the received signal lies in the noise. The attenuation is then decreased in steps to the point of receiver compression. This enables us to determine the linear range of system operation and to bias the system around the midpoint. At the bias point, a set of  $N$  impulse responses are collected and the input power level  $P_i$  recorded; the input power at the receiver antenna terminal is known from the power meter reading, the attenuator setting, and waveguide loss. In this way, a back-to-back calibration signal is calculated for all elements:

$$\begin{aligned} \hat{y}_i^{B2B}(t) &= \frac{1}{N} \sum_{j=1}^N \hat{y}_{ij}(t; g^{TX} = g_i^{RX} = 1, h_i(t) = \delta(t)) \\ &\approx p(t) * h^{TX}(t) * h_i^{RX}(t). \end{aligned} \quad (2)$$

Averaging is carried out to virtually eliminate noise such that the approximation above holds; we found that  $N = 256$  samples was sufficient.

The *calibrated* response is then obtained by deconvolving  $\hat{y}_i^{B2B}(t)$  from  $\hat{y}_i(t)$ :

$$\begin{aligned} y_i(t) &= \sqrt{\frac{P_i}{\frac{1}{T} \int_{t=0}^T |p(t)|^2 dt}} \cdot p(t) * \mathcal{F}^{-1} \left[ \frac{\mathcal{F}[\hat{y}_i(t)]}{\mathcal{F}[\hat{y}_i^{B2B}(t)]} \right] \\ &= p(t) * g^{TX} * h_i(t) * g_i^{RX} + n(t), \end{aligned} \quad (3)$$

with  $\mathcal{F}$  symbolizing the Fourier transform. Because the deconvolution effectively removes the pulse shape from the signal,  $p(t)$  must again be included, as given in (3). As well, the square-root scaling factor is required such that the power of  $y_i(t)$  corresponds to the power recorded when in calibration mode.

Referring to Figure 4, the ideal response of each element is the 2 GHz bandlimited pulse  $p(t)$ . The uncalibrated back-to-back response, however, contains the linear system effects, including pulse distortion and extraneous internal reflections. By applying the calibration in (3), the desired pulse is corrected and the linear distortion removed. Other experiments at NIST have revealed only small residual amounts of nonlinear distortion and noise remain. The calibration also accounts for the relative delay between the receive array elements. The worst case observed was 180 ps. On average, the slanted elements have 77 ps greater delay than the straight elements because they have longer waveguide connections. These relative channel delays were verified by means of VNA group delay measurements of the MUX subsystem.

### B. Clock Drift

The stability of a frequency source in the time domain is based on the statistics of its phase or frequency fluctuations over time. When using free-running clocks, we can predict the timing error of the clocks from the initial offset of the clocks,  $T_o$  (zero in our case because the clocks are initially synchronized with the PPS signal), the fractional frequency offset  $\Delta f/f$ , the aging rate (or frequency drift)  $D$ , and the noise deviation  $\sigma_x(t)$  over the calculation period. This relationship is expressed as [4]

$$\Delta T = T_o + (\Delta f/f) \cdot t + \frac{1}{2} D \cdot t^2 + \sigma_x(t). \quad (4)$$

In practice, the most significant source of timing error for our short measurement times is the fractional frequency offset, and so, to a first-order approximation, we use

$$\Delta T = (\Delta f/f) \cdot t. \quad (5)$$

From our clock specifications, often referred to as Stratum-1 or time stability holdover  $\Delta f/f = 10^{-11}$ . This means that at  $t = 60$  s,  $\Delta T = 600$  ps. Since we are using two clocks, they can be drifting in opposite directions, translating to a maximum drift of 1.2 ns/min. This calculation, however, does not take into account environmental fluctuations. In addition, the specifications supplied by the manufacturer are not measured over the time scale relevant to our application (on the order of minutes, not hours) and so just serve as a guideline.

Using the time-lag properties of the correlation and the position information provided by the robot, we can gauge our time drift when the robot is stationary or mobile. Through this analysis, we can see the actual time drift of our clocks and some of the environmental effects which can decrease clock stability (Figure 5). These data were collected during a measurement campaign over 4.1 minutes. Observe the slope change and level areas with small slopes where the robot

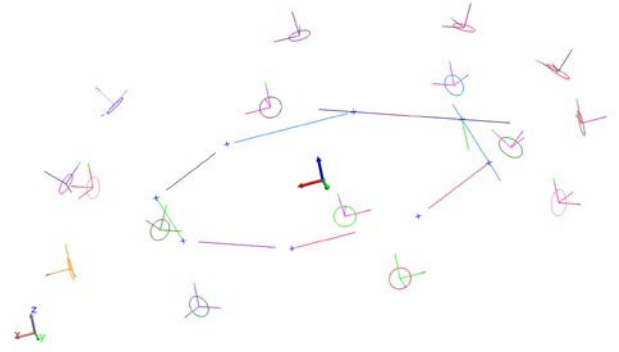


Figure 6. 28 GHz antenna aperture diagram. Data provide  $(r_i, \theta_i, \phi_i)$  for each element antenna aperture relative to the center of array body.

reaches a waypoint and subsequently pauses to download data. The total time drift was 9 ns or 2.20 ns/min.

Clock drift can affect the relative time-of-arrival estimates between antenna elements used to calculate angle-of-arrival. Specifically, it takes  $65.5 \mu\text{s}$  for a single channel measurement. Over that segment, the clock drift is only 0.0024 ps. If we use 2.20 ns/min, this equates to a phase error of 0.075 degrees at 83 GHz in  $65.5 \mu\text{s}$ . Hence, as described in the next section, this timing error is more than an order of magnitude less than the phase errors in our system calibration.

To gauge the actual properties of our clocks, we measured the frequency (or phase) drift of the clock versus a more stable reference available at NIST. The preliminary analysis results are complex and vary in time. A more complete analysis of the clocks will be undertaken in the future.

### C. Receiver Array Phase Centers and Antenna Patterns

Critical to the accurate estimation of AOA are the phase center locations of the array antennas. In order to precisely measure the constellation of the array elements with respect to its reference center, NIST has developed a near-field scanner which uses a laser interferometer capable of measuring the position of antenna apertures with an accuracy of 50 nm [6]. This translates to a phase accuracy of about 5 degrees at 83 GHz.

Figure 6 shows the array geometry as measured in the NIST antenna lab. With element  $i$  located at  $(r_i, \theta_i, \phi_i)$ , a multipath component approaching from angle  $(\theta, \phi)$  will hit the element with a relative delay of

$$\Delta \tau_i(\theta, \phi) = \frac{r_i}{c} \mathbf{x}(\theta_i, \phi_i) \cdot \mathbf{x}^T(\theta, \phi), \quad (6)$$

with respect to the array center, where  $\mathbf{x}(\theta, \phi) = [\cos \theta \cos \phi, \sin \theta \cos \phi, \sin \phi]$  and  $c$  is the speed of light.

Equally important to accurate AoA estimation is the angular response of the feed horn array. These horns have Gaussian beam patterns with equiphasic planes at radial offsets from the antenna's phase center. Once the positions of the antenna

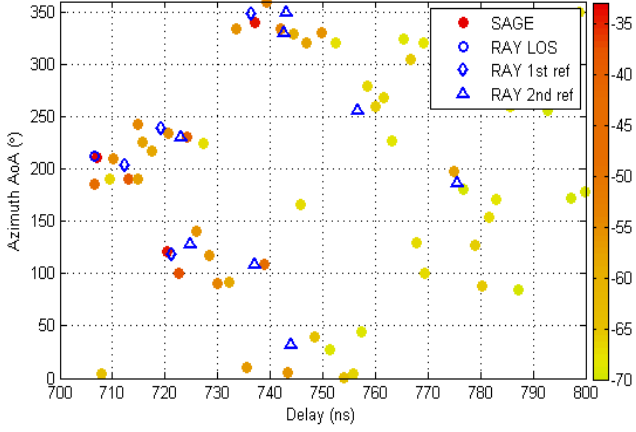


Figure 7. Multipath components extracted through the SAGE algorithm appear as color-coded solid circles vs. the dominant components predicted through raytracing shown in blue.

apertures, relative to the array center, are known, a near-field scan will be made for each of the 16 antenna elements. This scan will be made at three frequencies covering the 2 GHz bandwidth of the channel sounder at 1 degree angular spacing. We can transform the near-field data into the far field using methods developed by NIST and others [7,8]. These data will then provide the antenna phase centers relative to the antenna apertures and array center. They will also provide the measured amplitude and phase response of the antenna pattern. Because the transmit antenna has an omnidirectional pattern, its complex gain can be combined with the complex directional gain of the receive antenna as

$$g_i(\theta, \phi) = g^{TX} g_i^{RX}(\theta, \phi). \quad (7)$$

#### IV. MULTIPATH COMPONENT EXTRACTION

The channel impulse response for array element  $i$  can be expressed as the superposition of  $L$  multipath arrivals:

$$h_i(t; \zeta) = \sum_{l=1}^L \alpha_l \cdot \delta(t - \tau_l - \Delta\tau_l(\theta_l, \phi_l)). \quad (8)$$

In this notation, the channel is explicitly conditioned on the set  $\zeta = \{\zeta_1, \zeta_2, \dots, \zeta_L\}$ . The set contains the parameters  $\zeta_l = \{\alpha_l, \tau_l, \theta_l, \phi_l\}$  characterizing arrival  $l$  where  $\alpha_l$  is the complex amplitude,  $\tau_l$  the delay, and  $(\theta_l, \phi_l)$  the azimuth and elevation angles-of-arrival. By substituting (8) into (3), (3) can be rewritten compactly as

$$y_i(t) = \sum_{l=1}^L s_i(t; \zeta_l) + n(t), \quad (9)$$

where  $s_i(t; \zeta_l) = \alpha_l \cdot p(t - \tau_l) * c_i(\theta_l, \phi_l)$  is the  $l^{\text{th}}$  multipath pulse impinging on the  $i^{\text{th}}$  receive element and

$$c_i(\theta, \phi) = g_i(\theta, \phi) \cdot \delta(t - \Delta\tau_i(\theta, \phi)), \quad (10)$$

is the array “beamformer” given from (6) and (7).

We have implemented SAGE, an Expectation-Maximization (EM)-based algorithm, for the super-resolution<sup>1</sup> extraction of the multipath component parameters. In line with the notation in [5],  $y_i(t)$  in (9) represents the *observable* data. The objective of the algorithm is essentially to reconstruct  $y_i(t)$  as a composition of multipath pulses  $s_i(t; \zeta_l')$ . It proceeds by iterating on the parameter set  $\zeta'$  through maximum-likelihood estimation such that the residual, the noise  $n(t; \zeta')$ , obeys a Gaussian distribution.

Figure 7 displays the processed results for a single channel measured in a lab environment. Each solid circle represents a multipath component extracted with SAGE, shown only in azimuth vs. delay; the power is indexed according to the colorbar. Superimposed in blue are the LOS, 1<sup>st</sup>, and 2<sup>nd</sup> reflections predicted through simplistic raytracing modeling of the room as a parallelepiped. Considering the imprecisions of the model, good agreement is seen. The unmatched arrivals correspond to diffuse scattering clustered around the reflected paths as well as higher-order ( $> 2$ ) reflections.

#### V. CONCLUSIONS

Multiple channels sounders are being tested and deployed at NIST to support 5G channel model development. The probes span a frequency range from 28 to 83 GHz with bandwidths ranging between 2 GHz and 4 GHz. They are undergoing an extensive set of calibrations for the RF sections, timing sections, and antennas.

#### REFERENCES

- [1] T.S. Rappaport, S. Shu, R. Mayzus, H. Zhao, Y. Azar, K. Wang, G.N. Wong, J.K. Schulz, M. Samimi, and F. Gutierrez, “Millimeter wave mobile communications for 5G cellular: It will work!” *IEEE Access*, vol. 1, May 2013, pp. 335-349.
- [2] Papazian, P., Remley, K.A., Gentile, C., Golmie, N., “Radio Channel Sounders for Mobile Millimeter-Wave Communications: Angular Delay Spread and Doppler,” *Submitted for review*
- [3] J.A. Wepman, J.R. Hoffman, L.H. Loew, and V.S. Lawrence, “Comparison of wideband propagation in the 902-928 and 1850-1990 MHz bands in various microcellular environments,” *NTIA Report 93-299*, Sep. 1993.
- [4] Riley, W.J., “Handbook of Frequency Stability Analysis,” *NIST Special Publication 1065*, pp. 19, July 2008.
- [5] Hausmair, K., Witrisal, K., Meissner, P., Steiner, C., Kail, G., “SAGE Algorithm for UWB Channel Parameter Estimation,” *Proceedings of COST 2100 Management Committee Meeting*, Athens, Feb. 2010.
- [6] Josh Gordon, David Novotny, “High-Tech Measurements for High Frequency Antennas”, [http://www.nist.gov/ctl/rf-technology/rf\\_fields/robot-arm-aids-antenna-calibration.cfm](http://www.nist.gov/ctl/rf-technology/rf_fields/robot-arm-aids-antenna-calibration.cfm)
- [7] *IEEE Special Issue on Near-Field Scanning Techniques*, vol36, Issue 6, June 1988.
- [8] Near-Field Scanning Measurements: Theory and Practice, Michael Francis and Ronald Wittmann, pp. 929-976, 2008 Wiley and Sons

<sup>1</sup> Super-resolution because it yields a delay resolution above the 1 GHz bandwidth equivalent of 1 ns.